Clathrate $BaNi_2P_4$: An interplay of heat and charge transport due to strong host-guest interactions

Jian Wang,[a,b,#] Juli-Anna Dolyniuk,[c,#] Elizabeth Krenkel,[b,d,#] Jennifer L. Niedziela,[e,f,#] Makariy A. Tanatar,[b,d] Eric Timmons,[b,d] Tyson Lanigan-Atkins,[f] Haidong Zhou,[g] Yongqiang Cheng,[h] Anibal J. Ramirez-Cuesta,[h] Deborah L. Schlagel,[b] Udhara S. Kaluarachchi,[d] Lin-Lin Wang,[b] Sergey L. Bud'ko,[b,d] Paul C. Canfield,[b,d] Ruslan Prozorov,[b,d] Olivier Delaire,[e,f,i] Kirill Kovnir [a,b] *

[#] *Those authors contributed equally to the work*

[a] *Department of Chemistry, Iowa State University, Ames, IA 50011, United States*

[b] *Ames Laboratory, U.S. Department of Energy, Ames, IA 50011, United States*

[c] *Department of Chemistry, University of California, Davis, CA 95616, USA*

[d] *Department of Physics and Astronomy, Iowa State University, Ames, IA 50011, United States*

[e] *Materials Science and Technology Division, Oak Ridge National Laboratory, Oak Ridge, Tennessee, 37830, USA*

[f] *Department of Mechanical Engineering and Materials Science, Duke University, Durham, NC, 27708, USA*

[g] *Department of Physics and Astronomy, University of Tennessee, Knoxville, TN 37996 United States*

[h] *Neutron Scattering Division, Oak Ridge National Laboratory, Oak Ridge, Tennessee, 37830, USA*

[i] *Department of Physics, Duke University, Durham, NC, 27708, USA*

Abstract

Heat and charge transport properties of the metallic unconventional clathrate $BaNi_2P_4$, hosting Ba cations in oversized Ni_8P_{16} cages, are investigated. A novel method of single crystal growth was developed, yielding 2-3mm sized crystals of $BaNi_2P_4$. We also developed a setup to accurately measure thermal conductivity and electrical resistivity of the synthesized single crystals in a wide temperature range avoiding crystal remounting. $BaNi_2P_4$ has a metallic temperature dependence of its electrical resistivity (decreasing with decreasing temperature) and manifests an unconventional T^2 power law for 50 K < T < 300 K; below 50 K, the power law exponent increases gradually such that below 10 K the power law is T^5, a predicted but extremely rarely experimentally observed dependence for peculiar electron-phonon interactions. Electronic band structure calculations, consistent with measurements of de Haas-van Alphen oscillations, show large band dispersions with significant contributions of Ba orbitals to states near the Fermi level, which is atypical for clathrates. The thermal properties of $BaNi_2P_4$ were probed using a combination of variable-temperature single crystal X-ray diffraction experiments, heat capacity measurements, first-principles phonon dispersion calculations, and inelastic neutron scattering measurements. $BaNi_2P_4$ exhibits significant hybridization of the Ba-guest and Ni-P-framework vibrational modes, which may be enhanced via the detected split of the Ba position which results in strong Ba-framework interactions.

Introduction

Inorganic clathrates generally share a similar structural motif, incorporating large polyhedral cages with 20-28 vertices which can encapsulate guest cations or anions.[1,2] The guest species may rattle inside the cages or it can occupy several off-center positions. Large-amplitude anharmonic motions of the guest atoms tend to result in extremely low thermal conductivities compared to other crystalline solids.[1-4] The edges of the clathrate polyhedral cages correspond to covalent bonds between framework atoms. In conventional clathrates, the frameworks are based on group 14 elements – Si, Ge, and Sn. Many conventional clathrates are semiconductors and can be applied to the fields of thermoelectrics, photovoltaics, electrochemical energy storage, and gas storage.[1,2] A small subset of Ba-Si clathrates with metallic properties exhibit superconductivity due to unique host-guest interactions, namely hybridization of Ba5*d* and Si3*p* orbitals.[5,6] Exciting physical properties have been predicted for metallic clathrates containing rare-earth guests with partially filled *f*-shells, but due to the small size of rare-earth cations, only two reliable examples of Ce^{3+} guests have been reported,[7,8] whereas larger Eu^{2+} guests are more common.[9-12] In unconventional clathrates, the framework is based on a late- or post-transition metal and a pnictogen, group 15 element (P, As, and Sb).[4] Unconventional clathrates can be tuned to be semiconductors with outstanding charge transport properties.[3,4,8] The metallic unconventional clathrate $BaNi_2P_4$ attracted our attention due to an observed inconsistency in the thermal and electrical conductivities measured on sintered polycrystalline samples, indicating a possible violation of the Wiedemann-Franz (WF) law [13] $\kappa_E = LT/\rho$, where κ_E is the electronic contribution to the total thermal conductivity, ρ is electrical resistivity, L is the Lorentz number, and T is absolute temperature. For metals, L is close to the theoretical Sommerfeld value $L_0 = (\pi^2/3)(\kappa_B/e)^2 = 2.44\times10^{-8}$ $W\Omega K^{-2}$ where κ_B is the Boltzmann constant, and e is the charge of electron. This relation is strictly valid only at 0 K, because the value of L is obtained assuming that only electronic degrees of freedom remain at temperatures approaching 0 K, but is often used in the thermoelectric community to estimate the electronic contribution to the total thermal conductivity at finite temperatures. Total thermal conductivity is expected to be greater than just the electronic contribution due to thermal transport by phonons and magnons. Reported violations of the WF law occur at cryogenic temperatures.[14-17] A rare example of non-WF behavior above room temperature is metallic VO_2.[18] In VO_2 a strongly correlated electron fluid is present due to a

metal-insulator transition at 340 K, resulting in deviations from the Wiedemann-Franz law in the narrow temperature range of 340-390 K.

In our previous study,[19] the total experimental thermal conductivity measured on the sintered pellets of $BaNi_2P_4$ was lower than the electronic thermal conductivity estimated from the WF law (Figure S1). However, in those polycrystalline samples, grain boundaries may contribute at different relative strengths to phonon and electron scattering, thus both electrical resistivity and thermal conductivity measurements may be affected. In the current work, we grew single crystals of $BaNi_2P_4$ and measured their thermal conductivities, using a home-built apparatus, to show that the previously reported discrepancy is due to two-probe measurement errors. A detailed characterization of the transport properties of a single crystal of $BaNi_2P_4$ reveals this clathrate to exhibit a metallic temperature dependence of its electrical resistivity (decreasing with decreasing temperature). $BaNi_2P_4$ resistivity manifests a T^2 power law for 50 K < T < 300 K; below 50 K the power law exponent increases gradually such that below 10 K the power law is T^5. Computational and experimental explorations of electronic and phonon band structures reveal a hybridization of the guest Ba electronic and phonon states with the Ni-P framework modes which is atypical for clathrates.

Experimental

All handlings of the starting materials were performed inside an argon-filled glove box ($p(O_2) \leq 1$ ppm). The starting materials, metallic barium (Sigma-Aldrich, 99.9%), nickel powder (Alfa Aesar, 99.996%), copper powder (Sigma-Aldrich, 99.9%), red phosphorus (Alfa Aesar, 99%), and anhydrous nickel chloride (Alfa Aesar, 99%) were used as received. The single-phase polycrystalline samples of BaM_2P_4 (M = Ni, Cu) were prepared by solid-state reactions following the reported procedures.[19] Small $BaNi_2P_4$ crystals were also obtained from a metal-halide flux reaction in which $NiCl_2$ was used as a flux and a source of Ni. Ba metal, $NiCl_2$, and red P were combined in a 3:2:4 ratio and the same heating profile as the solid-state reaction of elements was used. The $BaNi_2P_4$ composition and absence of any Cl-containing inclusions was confirmed with SEM-EDS. Small (~0.005 mm^3) crystals of $BaCu_2P_4$ and small (~0.01 mm^3) crystals of $BaNi_2P_4$ were selected for variable temperature single crystal X-ray diffraction experiments.

Larger single crystals of $BaNi_2P_4$ were grown using a Seed-Aided Metal Flux method, which produced up to ~6 mm^3-sized single crystals and larger crystal agglomerates (Figure 1). For this technique, pre-synthesized single-phase powder of $BaNi_2P_4$ was sprinkled over silica wool and kept inside the top, inverted Al_2O_3 crucible. The reactants, Ba:Ni:P:Sn in 1:2:4:80 molar ratios using 30g of Sn, were loaded into the bottom Al_2O_3 crucible. The sealed ampoule was heated from room temperature to 1073 K at a rate of 30 K/h, then kept at this temperature for 240 h. Afterwards the ampoule was cooled down to 873 K over 40 h, annealed for 196 h at this temperature, and then the furnace was turned off. The ampoule was tapped several times during the cooling and annealing processes to drop the seed crystals into the bottom crucible and aid crystal growth. After annealing, the Sn flux was dissolved by treating the sample in a 1:1 HCl/water solution. A few selected crystals, out of many collected after this process, are shown in Figure 1. For transport property measurements, the crystals were polished to remove possible surface contamination. The compositions of crystals were confirmed by EDS to have no Sn or other impurities on the surface, such as chlorides from the HCl wash (Figure S5). Laue diffraction confirmed that the samples were high-quality single crystals (Figure S6).

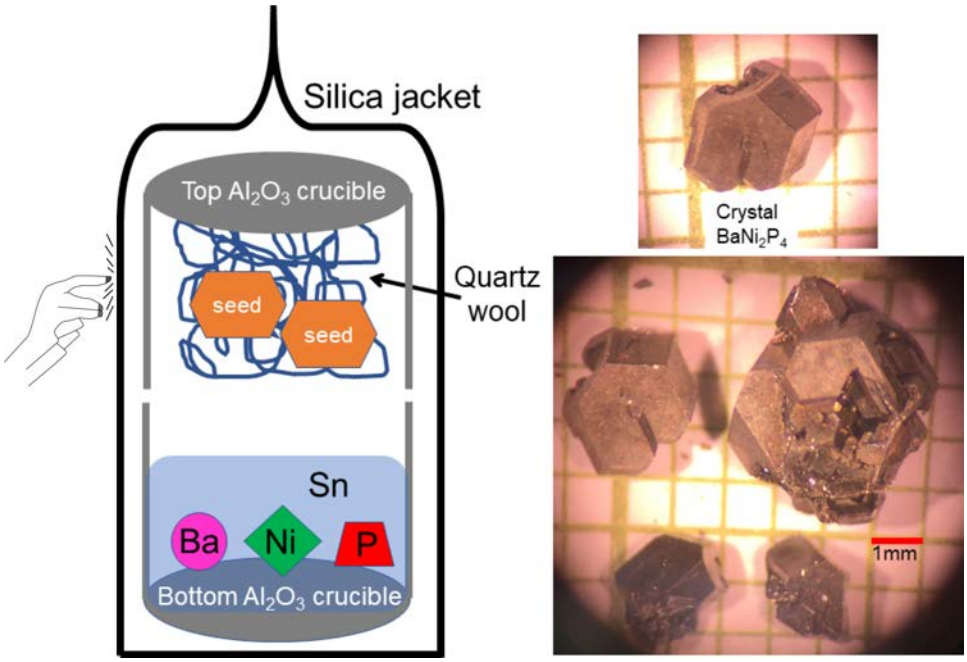

Figure 1. The set up for the Seed-Aided Metal Flux Method (left) and selected crystals of $BaNi_2P_4$ on the background of mm-grid paper (right).

Thermal conductivity measurements were performed using modular thermal conductivity (MTC) setups,[20] enabling measurements in several cryogenic environments, a cryogen-free He3 setup (0.5 to 3 K) and the high-vacuum option of a PPMS (above 2 K), without sample dismounting. A standard one-heater-two-thermometers technique was used for thermal conductivity measurements. The first MTC setup utilized RuO_2 thermometers and was constructed for measurements in the temperature range 0.02 to 40 K. The second setup used Cernox 1030 thermometers, suitable for measurements from 0.3 to 300 K. The calibration of the modular thermal conductivity setup with RuO_2 thermometers was described elsewhere.[20] The design with Cernox 1030 thermometers was specially built to study the properties of $BaNi_2P_4$ at elevated temperatures. This device was tested using measurements of standard Ag wire as shown in the supplementary material (Figure S4).

Samples for quantitative four-probe electrical resistivity and thermal conductivity measurements were polished from inner pieces of the single crystals in the shape of resistivity bars with typical sizes near (2-3)×0.5×0.1 mm^3. Contacts were made by soldering four 50 μm Ag wires to the samples using tin, similarly to iron-based superconductor samples.[21] Contact resistance was below 100 μΩ. Before mounting in the MTC apparatus, samples' resistivity measurements were pre-characterized to exclude those with tin flux inclusions. In order to measure both electrical resistivity and thermal conductivity on the same sample without dismounting from the MTC device, the high resistance wire of the thermal conductivity apparatus was temporarily shortened.[20] Use of the same sample in both measurements effectively diminished the uncertainty of geometric factor determinations in the two measurements.[20]

Magnetization measurements in the 1.8 – 300 K temperature range were performed using the VSM option of a Quantum Design Magnetic Property Measurement System (MPMS3). The sample was mounted on a quartz sample holder that has virtually no background.

Further details on the characterization techniques used are provided in the supporting information, including variable temperature single crystal X-ray diffraction, heat capacity, calculations, and inelastic neutron scattering measurements.

Results and discussion

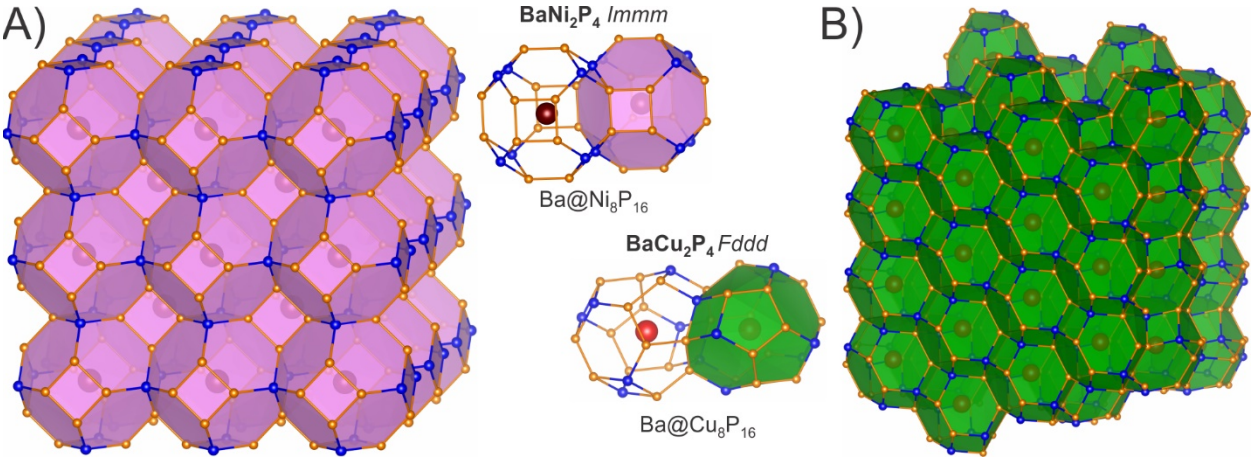

Figure 2. Polyhedral representation and two cages fused via hexagonal faces in the crystal structures of (A) $BaNi_2P_4$ and (B) $BaCu_2P_4$. Ba: large spheres; Ni or Cu: small blue spheres; P: small orange spheres.

We have recently reported the synthesis and basic properties of $BaNi_2P_4$ and $BaCu_2P_4$ clathrates,[19] where Ba cations are enclosed either in a truncated Ni_8P_{16} octahedra (Figure 2A) or in Cu_8P_{16} twisted polyhedra (Figure 2B). $BaCu_2P_4$ exhibits properties typical for clathrates.[19] In turn, the polycrystalline sintered pellets of $BaNi_2P_4$ were reported to violate WF law with a smaller total thermal conductivity than the estimated electronic contribution. To verify that this observation is not due to the polycrystalline nature of the samples, large single crystals of $BaNi_2P_4$ were grown by a newly-developed Seed-Aided Metal Flux method (Figure 1). Thermal conductivity measurements on large single crystals using a PPMS TTO two-leads method confirmed the anomalously low total thermal conductivity of less than 5 $Wm^{-1}K^{-1}$ (Figure S2). However, the two-leads option may underestimate thermal conductivity and is not recommended in the Quantum Design PPMS TTO manual for samples with expected thermal conductivities exceeding 10 $Wm^{-1}K^{-1}$.[22]

After calibration of our home-built four-probe thermal conductivity setup with Ag (Figure S4), measurements were performed on a $BaNi_2P_4$ single crystal. Figure 3 shows a comparison of the temperature-dependent thermal conductivity, κ, of $BaNi_2P_4$ measured using a RuO_2 MTC device (red triangles), a Cernox 1030 MTC device (blue squares), as well as the thermal conductivity calculated from resistivity data using the equation L_0T/ρ (see Figure 4a below). The inset shows a

zoomed-in view of the low-temperature portion of the same data plotted as κ/T vs T. The thermal conductivity and resistivity saturate at low temperatures in the residual resistivity range and converge to obey WF law. At temperatures as high as 40 K, the thermal conductivity remains very close to the value calculated from the electrical resistivity. Note, that both measurements, resistivity and thermal conductivity, were performed on the same setup without sample dismounting, thus minimizing potential dimensional measurement errors. The mismatch for the resistivity-derived WF thermal conductivity and the PPMS experimental thermal conductivity was thus not confirmed (Figure S3). A significant underestimation of the thermal conductivity of metallic $BaNi_2P_4$ in PPMS measurements can be attributed to the two-probe geometry used.

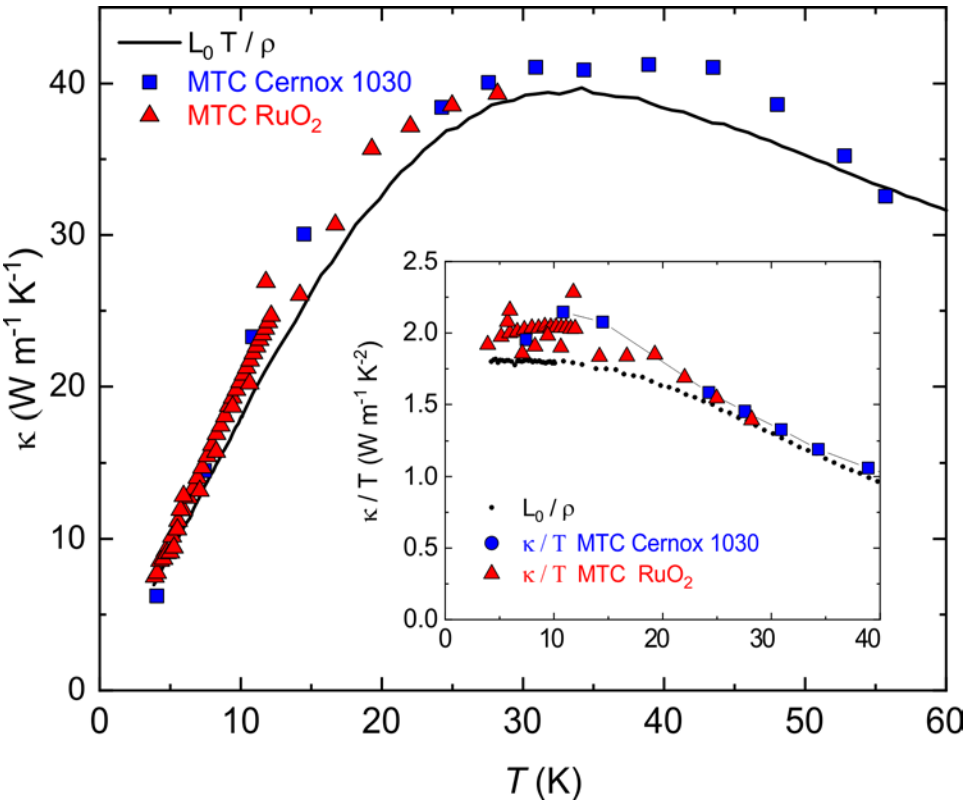

Figure 3. Temperature dependences of the thermal conductivity for single crystal of $BaNi_2P_4$: experimentally measured with a MTC Cernox 1030 (blue squares), a MTC RuO_2 (red triangles), and calculated from resistivity using WF law (black line). Inset shows κ/T dependences in the low-temperature region.

For the $BaNi_2P_4$ single crystal, an estimate of the phonon contribution to the thermal conductivity in the 20-35 K range is calculated to be ~2 $Wm^{-1}K^{-1}$, as the difference between the total thermal

conductivity and the electronic contribution estimated from resistivity data. The 20-35 K temperature range was chosen where two MTC datasets show consistent values. A lattice thermal conductivity of ~2 $Wm^{-1}K^{-1}$ is comparable to the lattice thermal conductivity of sintered pellets of $BaCu_2P_4$, which is 1.7 $Wm^{-1}K^{-1}$ at 35 K,[19] and to other transition metal-phosphorus clathrates, 0.5-3 $Wm^{-1}K^{-1}$ at similar temperatures.[3,4,8,23-25]

A more quantitative comparison of thermal and electrical channels can be performed using the temperature-dependent parts of both quantities. In Figure 4A we compare $\rho(T)$ of $BaNi_2P_4$ with a standard temperature-dependent resistivity of a good metal, represented by Ag, plotting both datasets with the resistivity value at room temperature, ρ(300 K) normalized to 1. The resistivity of $BaNi_2P_4$ is strikingly different from the usual T-linear dependence expected for metals with dominant phonon scattering. To better quantify the temperature dependence of the resistivity we plot the change in resistivity $\rho(T) - \rho(0K)$ on a double log scale (main panel of Figure 4B). Such a plot reveals power-law-like behavior and, in the case of $BaNi_2P_4$, shows that at the lowest temperature the T^n power law is close to $n = 5$ (inset in the Figure 4B) and that as temperature increases to $T \sim 50$ K, n decreases to ~2. Indeed, for 50 K < T < 300 K the change in resistivity has close to a T^2 temperature dependence. Due to the noise in the data in the low temperature regime and the uncertainty of ρ_0, we cannot exclude the possibility of other high-power functions, however T^4 and T^6 functions give worse fits. The plot shows that the crossover from dominant T^5 to T^2 dependence (lines in the panel) is gradual and there is no extended range of any dependence.

The $\rho \sim T^5$ is a theoretically expected but this dependence is very rarely experimentally observed.[26] It is expected in the range of dominant contributions of long-wavelength phonons to heat capacity and thermal conductivity, is responsible for a T^3 dependence, and simultaneously to scattering of conduction electrons. The actual cause of the difference in power laws is the inability of the small angle scattering events of these phonons to degrade charge current, so that Umklappp scattering events are required.[26]

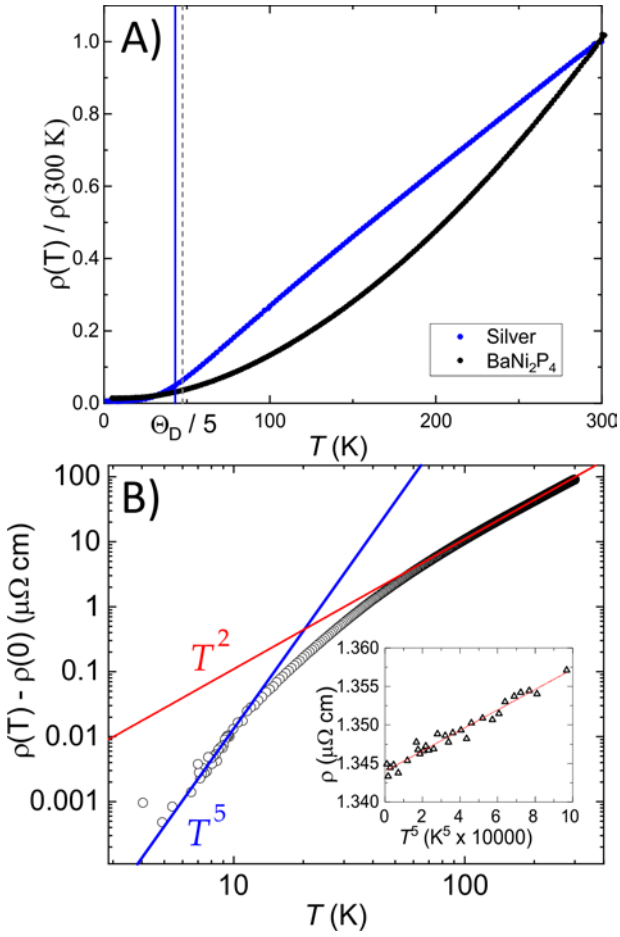

Figure 4. Temperature dependences of the resistivity of a $BaNi_2P_4$ single crystal: (A) Comparison of $BaNi_2P_4$ resistivity (black line) to that of silver metal (blue line). Note, that $BaNi_2P_4$ Debye temperature is close to that of Ag (Table 1), vertical lines (solid line for $BaNi_2P_4$, dashed line for Ag) of corresponding color show the magnitude of $\Theta_D/5$ for both compounds. (B) Log-log plot of the inelastic part of electrical resistivity $\rho(T)-\rho(0K)$ vs. temperature. Blue and red lines show T^5 and T^2 functions, correspondingly, inset shows fit of the lowest temperature portion of $\rho(T)$ using ρ vs. T^5 plot.

The usual interpretation of the $\rho(T) = \rho_0 + AT^2$ temperature dependence is the dominance of electron-electron scattering processes in the Landau Fermi liquid model, which is premised on the T^2 behavior extending to the lowest temperatures, which is clearly not the case here (as shown in Figure 4B). In our case, the range of T^2 dependence starts somewhere close to 50 K and thus is disconnected from the lowest temperatures, so a different mechanism should be invoked.

The vibrational dynamics of the guest atoms and the thermal behavior in $BaNi_2P_4$ were further studied and compared with those in $BaCu_2P_4$ which exhibits properties typical of clathrate

compounds. Variable-temperature single crystal X-ray diffraction shows no structural transitions for $BaCu_2P_4$ in the 10-230 K temperature range (Tables S1 and S3). The refinement of the 10 K dataset reveals that Ba anisotropic displacement parameters (ADPs) are comparable to those for framework Cu and P atoms and there is no extra electron density in the vicinity of the Ba cation in the center of $[Cu_8P_{16}]$ cage. This is in contrast to Si-, Ge-, and Sn-based clathrates where large ADPs for the guest atoms in the 24-vertex cages are maintained even at low temperatures or displacements of the guest cations from the center of the cage were reported.[24,27] A refinement of the $BaNi_2P_4$ crystal structure identified extra electron density peaks in the vicinity of the Ba site which we attribute to a splitting of the Ba site. These peaks were best resolved for the 10 K dataset where thermal motion was minimized. For the 10 K data, the first residual electron density peak is ≈2.5 times larger than the second or third residual peaks. This partially occupied Ba11 atomic site (5% occupancy) of 24*k* symmetry is located at a short, physically impossible, distance of 0.63 Å from the original *2a* Ba1 site (95% occupancy), suggesting a Ba site splitting (Figure 5A and S7).

Four Ba11 sites form a rectangle in the *bc*-plane parallel to the P_4 square face of the truncated octahedron (Figure 5A and Table S2). Ba1 is located in the center of a P_8 square prism with Ba1-P distances of 3.28-3.29 Å and the shortest Ba1-Ni distance is 3.46 Å. The Ba11 is shifted towards a Ni_2P_2 square face, which results in substantial shortenings of the Ba11-P (3.01-3.13 Å) and Ba11-Ni (3.07-3.28 Å) distances. Both Ba11-P and Ba11-Ni distances are compared with the shortest corresponding distances reported for $Ba_7Ga_4P_9$ (Ba-P = 2.959 Å), $Ba_5P_5I_3$ (Ba-P = 3.044 Å), and $BaNi_2Ge$ (Ba-Ni = 3.096 Å).[28-30] Such short distances in $BaNi_2P_4$ may indicate weak bonding interactions similar to the recently detected host-guest Ba-Au interactions in the $Ba_8Au_{5.3}Ge_{40.7}$ clathrate.[31]

$BaCu_2P_4$ exhibits gradual thermal expansion (Figure 5C and Table S1) and temperature behavior of its ADPs (Figure 5B). In contrast, $BaNi_2P_4$ exhibits a significant shrinkage between 90 K and 10 K (Figure 5C and Table S1), a behavior atypical for solids, likely related to the off-centering of the Ba ions. The Ba ADPs' behavior in $BaNi_2P_4$ confirms the observed splitting of Ba sites. Indeed, when a model without splitting is considered, the Ba ADPs at 10 K are abnormally high (Figure 5B). Including the split position results in a linear temperature dependence of the Ba ADPs.

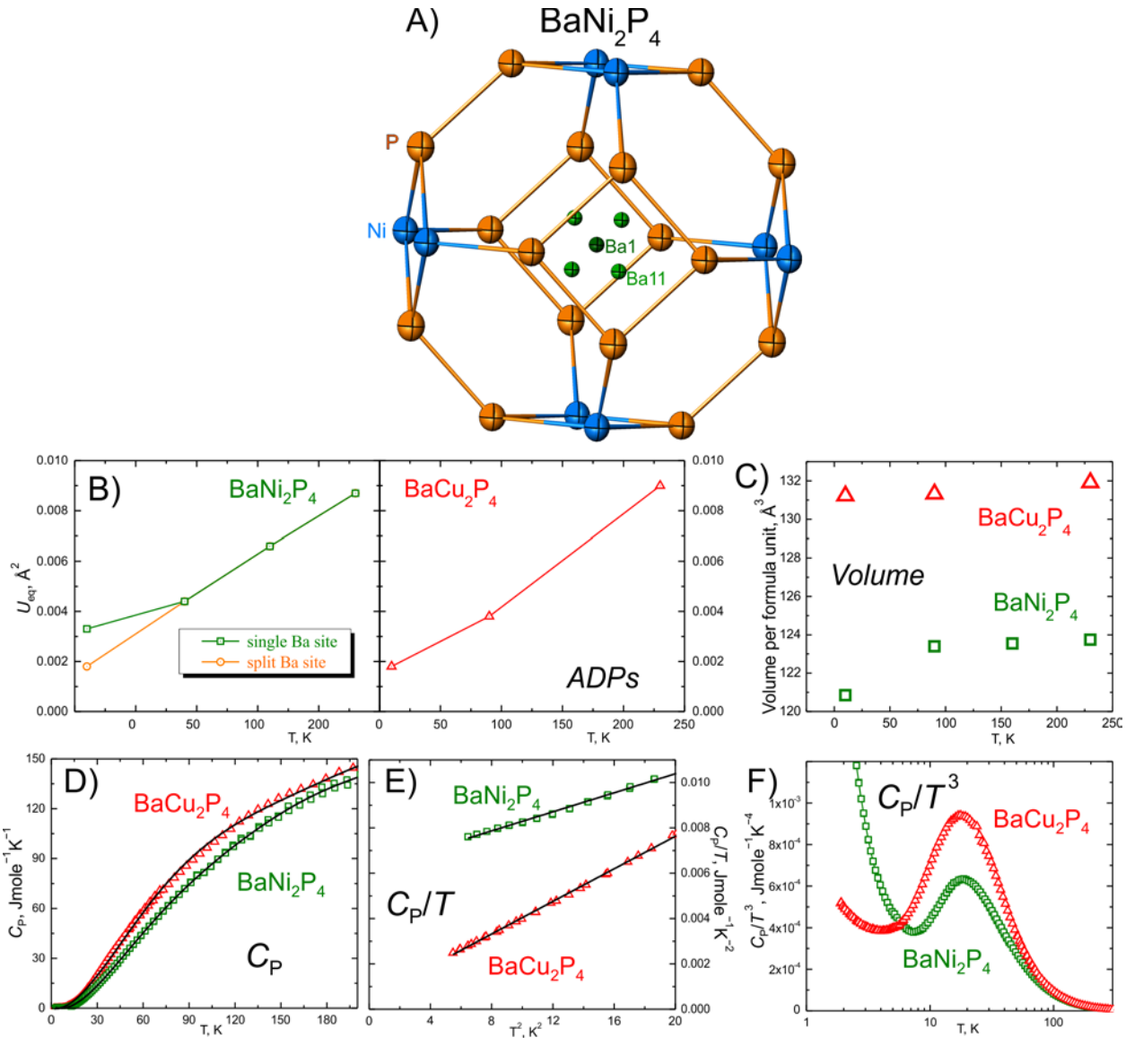

Figure 5. (A) Split Ba sites in the crystal structure of $BaNi_2P_4$ at 10 K, Ba1 is in the center of the cage, while Ba11 is displaced from the center and has 4 symmetry equivalent sites. Thermal ellipsoids are drawn with 99% probability. Ba: green; Ni: blue; P: orange. Temperature dependences of (B) the equivalent ADPs of guest Ba atoms and (C) the volume per formula unit. Estimated standard deviations are smaller than the symbol size used. (D) Heat capacity for $BaNi_2P_4$ and $BaCu_2P_4$. Experimental data are shown with symbols and solid lines represent fits using two Einstein modes. (E) The low-temperature heat capacity data represented as C_P/T vs. T^2. (F) The same represented as C_p/T^3 *vs. T*. Derived Debye and Einstein temperatures are given in Table 1.

The heat capacity measurements show smooth, phase transition-free, curves (Figure 5D). This indicates that $BaNi_2P_4$ is not a two-level system with a thermally induced population of Ba11 sites. Estimates of the Sommerfeld coefficients (Figure 5E and Table 1) agree with electronic structure

calculations where $BaCu_2P_4$ was predicted to have much lower density of states per atom at the Fermi level compared to $BaNi_2P_4$.[19]

Table 1. Physical parameters for BaM_2P_4 derived from ADPs and heat capacity data. γ: Sommerfeld coefficient, θ_D: Debye temperature; θ_E: Einstein temperature.

	γ, $mJmol^{-1}K^{-2}$	β, $mJmol^{-1}K^{-4}$	θ_D, K		θ_E, K	
			ADP	C_P	**ADP**	C_P
$BaCu_2P_4$	0.45(2)	0.359(2)	233(5)	175(1)	135(5)	60(1), 125(1)
$BaNi_2P_4$	5.99(4)	0.226(3)	237(5)	205(1)	137(5)	64(1), 124(1)

Recently, a heat capacity investigation of $BaNi_2P_4$ was reported which qualitatively agrees with our studies.[32] Their reported positive slope for C_P/T *vs.* T^2 in $BaNi_2P_4$ at $T^2 < 25\ K^2$ is distinct from our observations. No such anomalies were observed in our studies (Figures 3E) which indicate that the reported low-temperature features may not be intrinsic for $BaNi_2P_4$. The discussed low-temperature features affect the estimation of Debye temperatures which were reported as high as $\theta_D = 500$ K for $BaNi_2P_4$,[32] in contrast to our results of 205 K (Table 1). We cross-verified the Debye temperatures derived from the heat capacity measurements with the Debye temperatures estimated from the variable temperature diffraction experiments (Table 1). Based on relatively good agreement between the two methods, we consider the reported θ_D values of 500 K as an overestimation.

The plots of C_P/T^3 *vs.* T show distinct peaks above 5 K, characteristic of Einstein oscillators (Figure 5F and Table 1). To assess whether the vibrations of guest atoms are decoupled from those of the framework, a detailed study of the phonons was performed. In the calculated phonon density of states (PDOS) curves, each of the different atom types contributes to distinct spectral regions (Figures 6A and 6B). The heavy guest atom (Ba) contributes primarily to the low-frequency region (below ~120 cm^{-1}), the Cu or Ni vibrations dominate the intermediate frequencies (~100 to 300 cm^{-1}), and the light P atoms dominate the high-frequency range of the spectra. In the calculation for $BaNi_2P_4$, guest atom splitting was ignored, and the calculation was performed on the idealized structure with a single, centered Ba site.

The low-energy vibrations of $BaCu_2P_4$ have very little contribution from the Cu-P framework, while the higher energy Ba vibrations overlap in energy with the framework Cu and P vibrational

modes. For $BaNi_2P_4$, the Ba vibrations show a more pronounced overlap with framework vibrations, which is also visible from the phonon dispersion plot. Upon comparison of $BaCu_2P_4$ and $BaNi_2P_4$, significant differences can be seen between the two PDOS spectra. The Cu partial DOS is constrained to the 80-160 cm^{-1} region while the Ni partial DOS spreads over a much larger energy range, 60-340 cm^{-1}. Some of those vibrations can be detected by Raman spectroscopy on a crystal of $BaNi_2P_4$, where four peaks corresponding to Ni-P and P-P vibrational modes with energies of 154, 284, 356 and 456 cm^{-1} were present (Figure S8).

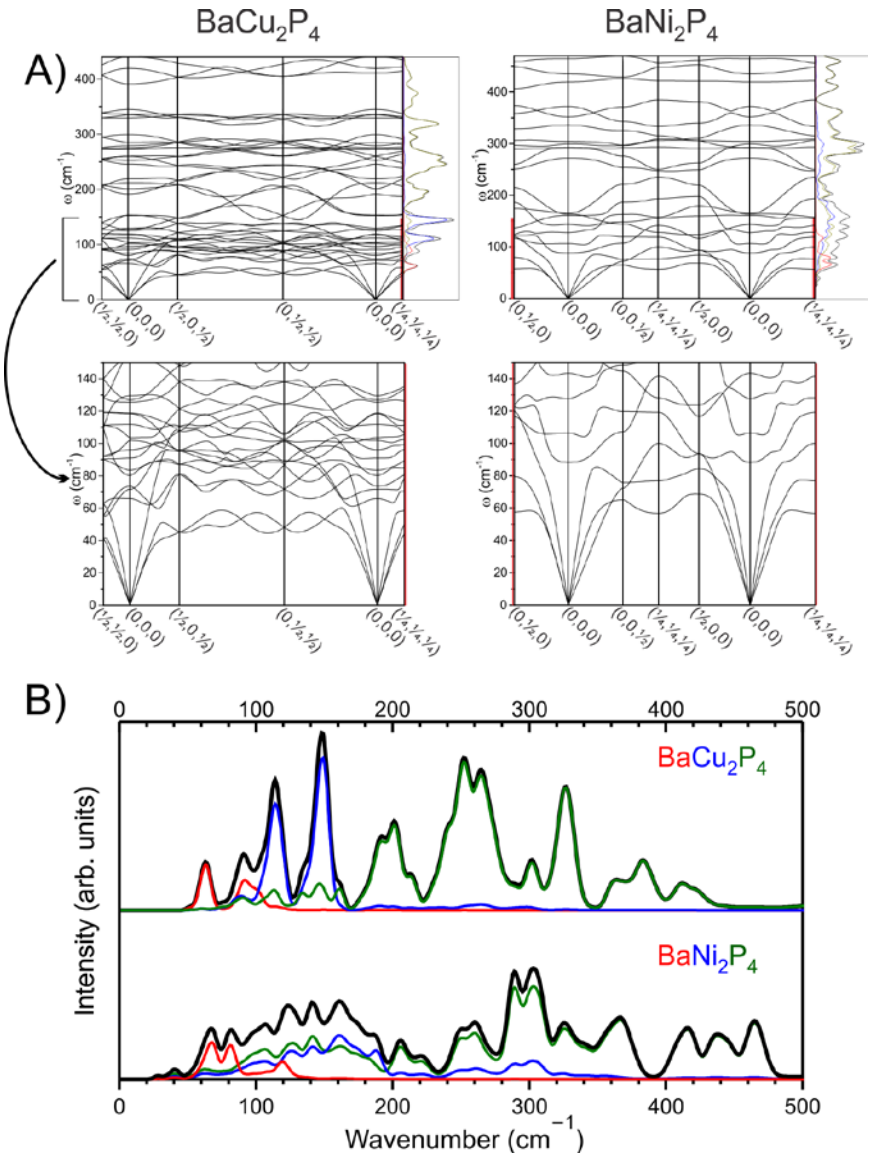

Figure 6. (A) Phonon dispersion and (B) density of states calculations for the BaM_2P_4. Ba contributions: red; Cu and Ni: blue; P: green.

The experimental PDOS of $BaNi_2P_4$, extracted from INS measurements of a polycrystalline sample, is consistent with the simulations (Figure 7). We note that the low-energy portion of the PDOS shows a stiffening with increasing temperature and non-Debye behavior for temperatures less than 100 K, possibly reflecting anharmonicity of Einstein-like modes, related to uncorrelated Ba ionic motions within the Ni-P framework below 100 K. The rest of the PDOS shows little change upon warming, showing that the Ni-P framework is more harmonic and less sensitive to thermal changes. To gain a deeper understanding of the phonon dispersions significantly larger crystals, 1-2 cm^3, are required.[31]

The calculated phonon dispersions for $BaNi_2P_4$ (Figure 6A) do not show clear Einstein-like modes at low energy unlike those seen in many other clathrates.[33] Instead, the acoustic branches bend down into flatter dispersions. Ba vibrational amplitude dominates the flat regions at the top of acoustic branches as well as some low-energy portions of optical branches, which supports the notion of low-energy, large-amplitude Ba vibrations. However, since the Ba modes are clearly hybridized with acoustic modes, there is not a distinct decoupling into Ba modes *vs.* framework modes. $BaNi_2P_4$ exhibits a splitting of the Ba position, resulting in short Ba-framework interactions. Unlike in $BaCu_2P_4$, the Ba vibrations in $BaNi_2P_4$ do not result in flat guest optical modes. Instead, a partial hybridization of the Ba and Ni-P framework vibrational modes is predicted computationally, with the associated DOS matching the experiments well.

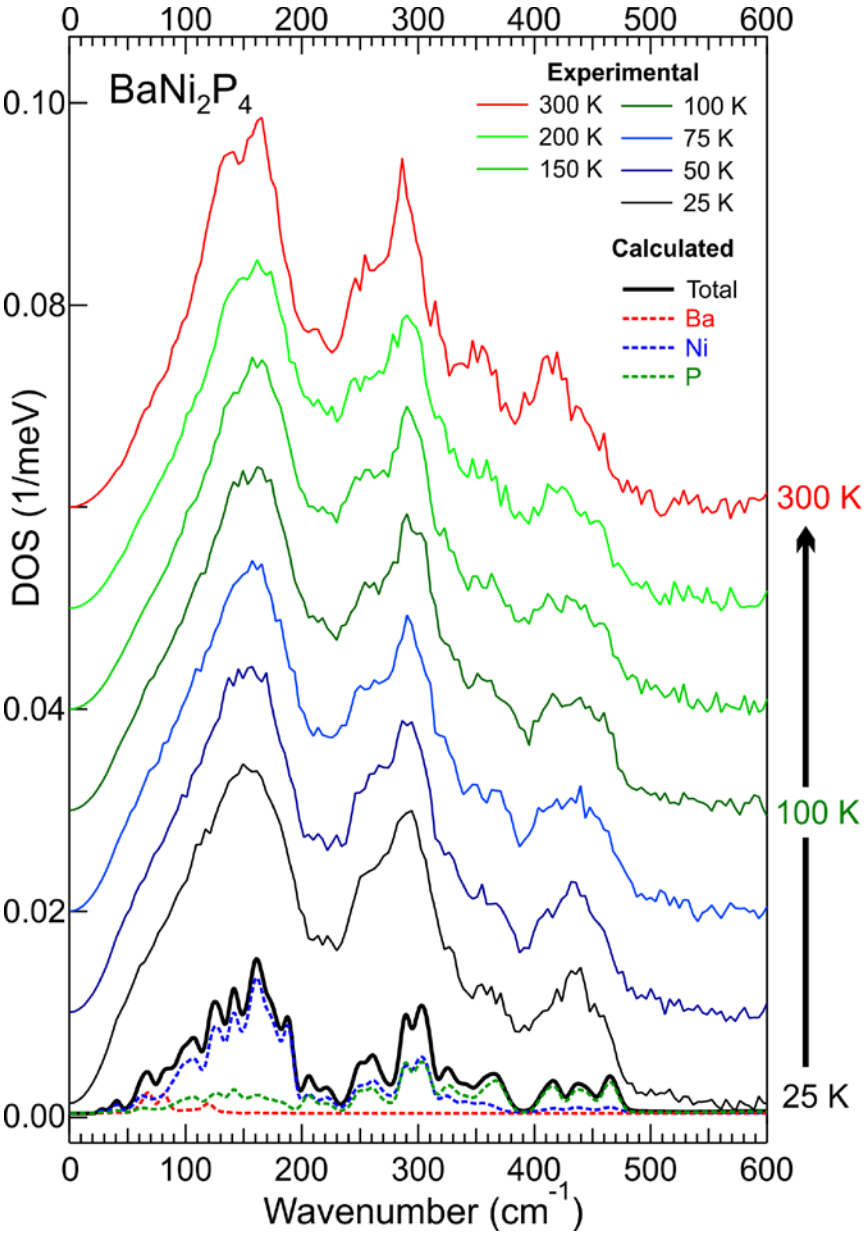

Figure 7. Neutron-weighted phonon density of states extracted from inelastic neutron scattering data as a function of temperature. Curves are offset for clarity. The bottom plot is a calculation weighted by neutron cross-section PDOS for $BaNi_2P_4$.

In most clathrates, the contribution of guest atoms to the electronic states near the Fermi level is minimal.[1,2] This is not the case for $BaNi_2P_4$. The electronic band structure of $BaNi_2P_4$ calculated with DFT using the PBE functional, including spin-orbit coupling (SOC) is presented in Figure 8. From the band dispersion (Figure 8A), below the Fermi energy (E_F) the valence bands from E_F–2.0 to E_F–1.0 eV are mostly of Ni 3*d* character and relatively localized, with limited dispersion. In

contrast, the valence bands from E_F–1.0 to E_F+0.5 eV are mostly derived from P 3*p* and some Ni 3*d* orbitals, and are less localized, exhibiting stronger dispersion. The lowest conduction band spans a large energy range from E_F–0.5 to E_F+1.0 eV and contains a mixture of contributions from Ba *s* and P p_y as well as some Ni d_{z2} and d_{x2-y2} orbitals. Among the three bands crossing E_F, two are hole bands and one is an electron band. The 3D Fermi surface is shown in Figure 8B. The lower-energy hole band forms a small pocket (green) around the *X* point, along the orthorhombic [100] direction. The higher-energy hole band forms multiple pockets (blue) mostly near the Brillouin zone boundaries. In contrast, the conduction band forms a large electron pocket (cyan) with a cubic shape around the zone center mostly and an additional small electron pocket at *T* point.

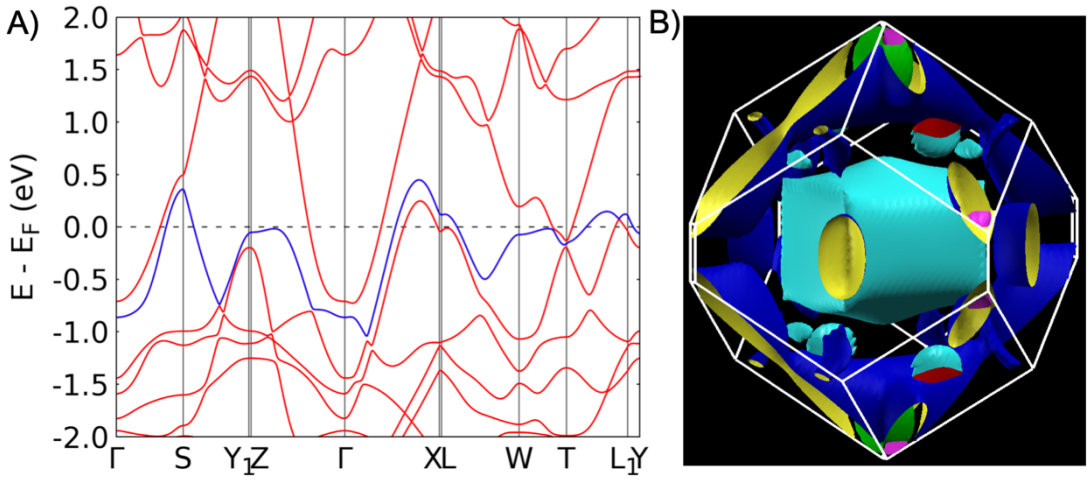

Figure 8. Electronic band structure of $BaNi_2P_4$. (A) Band dispersion with the top valence band according to the simple band filling in blue. (B) Fermi surface with two hole bands (green and blue) and one electron band (cyan).

To verify predicted band structure magnetic properties of $BaNi_2P_4$ were characterized. Figure 9 presents the results of magnetic measurements on $BaNi_2P_4$ between 1.8 and 300 K. Magnetization isotherms, M(H), presented in the inset, have several features: the measurements at 1.8 K show quantum oscillations (vide infra). All M(H) measurements display a quick rise (in fields up to 10 kOe in the first quadrant) followed, for 50 K ≤ T ≤ 300 K, by essentially linear M(H) . This behavior suggests a contribution of small, on the order of $4x10^{-5}$ μ_B/mol, ferromagnetic (or

ferromagnetic and paramagnetic) impurities. In such a case, the contribution of impurities to the temperature dependent susceptibility of the sample can be eliminated by approximating the magnetic susceptibility as $\chi = (M_1-M_2)/(H_1-H_2)$ where H_1 and H_2 correspond to the linear region of M(H).

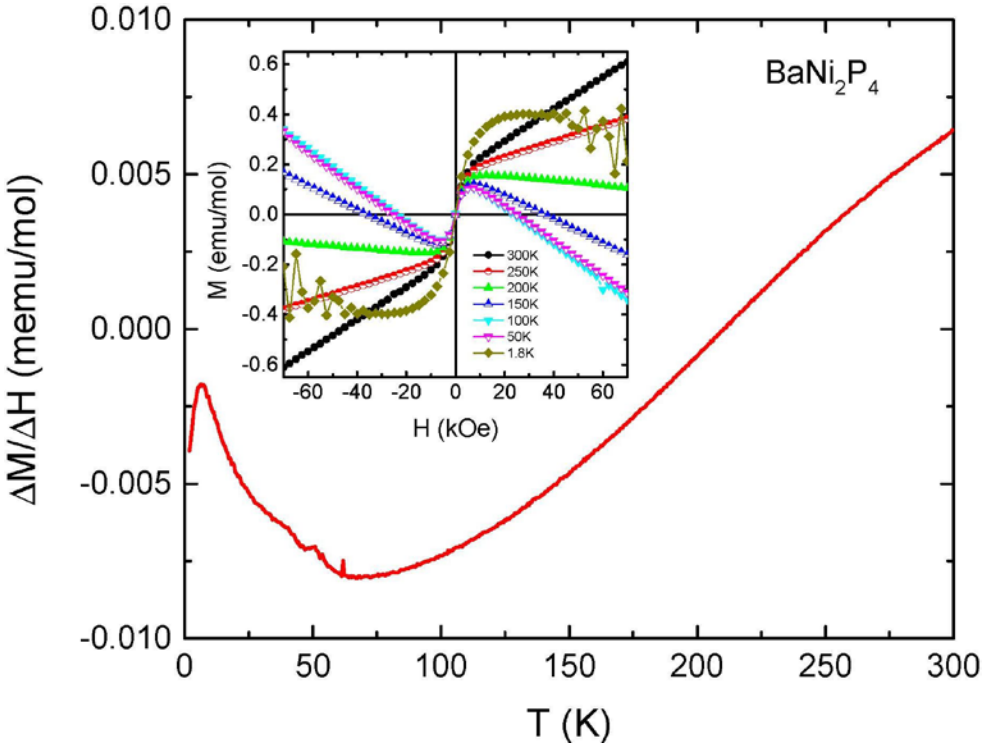

Figure 9. Temperature dependent magnetic susceptibility of $BaNi_2P_4$ determined as $\Delta M/\Delta H = (M_1-M_2)/(H_1-H_2)$, where H_1 = 70 kOe, H_2 = 25 kOe (see the text). Inset: Field dependent magnetization measured at constant temperatures between 1.8 K and 300 K.

The magnetic susceptibility plotted in Figure 9 results from the measurements at 25 kOe and 70 kOe. The values of susceptibility are small. $BaNi_2P_4$ is paramagnetic at room temperature. On cooling, susceptibility decreases and changes sign to diamagnetic at ~ 200 K. The apparent peak at ~ 7 K is probably an artifact of quantum oscillations observed at low temperatures.

The field dependent magnetization of $BaNi_2P_4$ was measured between 20 kOe and 70 kOe at several different temperatures (Figure 10A). De Haas-van Alphen (dHvA) oscillations are clearly

seen above ~30 kOe in the 1.8 K data. There oscillations persist at least up to 7 K. The results of the Fast Fourier Transform (FFT) of the 1.8 K magnetization data plotted as M vs. 1/H are shown in Figure 10B. A dominant dHvA frequency is observed at 2.85 MG, significantly smaller FFT peaks can be seen at 5.2, 6.4, and 9.3 MG (labeled with asterisks in figure 10B). Further work is needed to confirm whether those smaller peaks really correspond to dHvA oscillations or are the result of a peculiar noise.

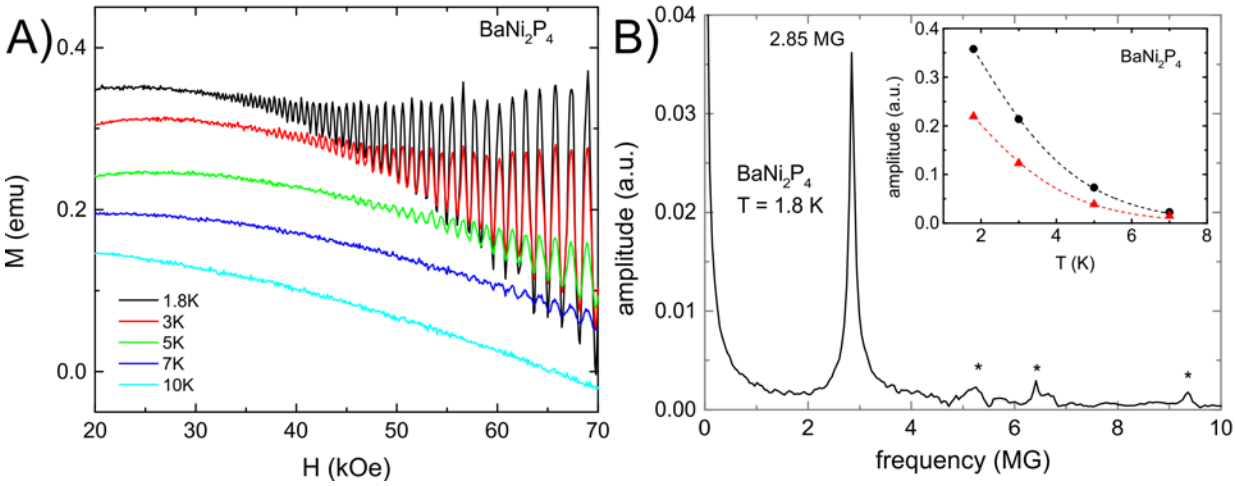

Figure 10. A) Field-dependent magnetization of $BaNi_2P_4$ measured at several temperatures between 1.8 K and 10 K. B) FFT of the field-dependent magnetization data at 1.8 K plotted as M vs. 1/H. Inset: symbols are the amplitude of the dHvA oscillations at two different values of magnetic field, dashed lines are Lifshitz-Kosevich fits.

The effective mass corresponding to the dominant dHvA frequency can be determined by fitting the temperature-dependent amplitude of the dHvA oscillations, R_T, to the Lifshitz-Kosevich formula:

$$R_T = \frac{X}{\sinh X} \quad X = \frac{2\pi^2 k_B m_e}{\hbar e}\frac{m^* T}{B}$$

where m^* is effective mass in units of the electron mass, m_e, T is temperature, and B is applied magnetic field. The data and fits for two different magnetic field values are shown in the inset to Figure 10, which yield $m^* \sim 0.37\ m_e$. The small hole pocket (green) of the DFT-calculated Fermi surface in Figure 8B gives a dHvA frequency of 2.73 MG for the magnetic field along the

orthorhombic [100] direction, which agrees with the experimental result. The associated effective mass of 0.12 m_e is smaller than the measured value.

Conclusions

The present study included the growth of large single crystals of $BaNi_2P_4$ and the development of a home-made setup to properly evaluate the thermal conductivity of few mm-sized single crystals. No significant deviation from the Wiedemann-Franz law was observed in the present study. Metallic $BaNi_2P_4$ exhibits properties orthogonal to what is commonly expected for clathrates: a strong hybridization of guest electronic and vibrational states with states of the clathrate framework and a strong interplay of heat and charge transport. A tunability of such peculiar host-guest interactions in $BaNi_2P_4$ will be probed in the course of future work.

Supporting Information

Experimental details, figures, and tables pertinent to characterization techniques used: spark plasma sintering, transport properties measurements and calibration, Laue diffraction, variable temperature single crystal X-ray diffraction and difference electron density maps, heat capacity, phonon and electronic band structure calculations, energy dispersive X-ray spectroscopy, inelastic neutron scattering and Raman measurements. This material is available free of charge via the Internet at http://pubs.acs.org.

Acknowledgements

The authors wish to thank Dr. S.M. Kauzlarich at UC Davis and Dr. J. Zaikina at Iowa State University for use of SPS; and Dr. Håkon Hope (deceased) and Dr. James Fettinger at UC Davis for help with 10 K diffraction experiments.

AUTHOR INFORMATION

Corresponding Author: kovnir@iastate.edu

Author Contributions

All authors have given approval to the final version of the manuscript.

Authors declare no competing financial interests.

Funding Sources

This research was primarily supported by the U.S. Department of Energy, Office of Basic Energy Sciences, Division of Materials Sciences and Engineering. Synthesis, crystal growth, and structural analysis as well as preliminary PPMS-based properties measurements by JW, JD, and KK were supported under Award DE-SC0008931. Resistivity and thermal conductivity measurements by EK, ET, MAT, and RP, Laue diffraction studies by DLS, band structure calculations by LLW, heat capacity studies by UK, magnetization measurements by SLB, as well as careful analysis of the transport data by PCC were performed at Ames Laboratory which is operated for the U.S. DOE by Iowa State University under contract #DE-AC02-07CH11358. Neutron scattering measurements by JLN and OD were supported by the S3TEC EFRC, an Energy Frontier Research Center funded by the U.S. Department of Energy, Office of Science, Basic Energy Sciences under Award DE-SC0001299. Raman measurements by TLA were supported by the U.S. Department of Energy, Office of Science, Basic Energy Sciences under Award DE-SC0019299. JD acknowledges the DOE-SCGSR fellowship for time spent at Oak Ridge National Laboratory. This research used resources at the Spallation Neutron Source operated by the Oak Ridge National Laboratory, which is sponsored by the Scientific User Facilities Division, Office of Basic Energy Sciences, U.S. Department of Energy. The computing resources were made available through the VirtuES project, funded by the Laboratory Directed Research and Development (LDRD) program at ORNL.

References

1. *The Physics and Chemistry of Inorganic Clathrates*. Ed.: Nolas, G. S. Springer, New York: 2014.

2. Dolyniuk, J.-A.; Owens-Baird, B.; Wang, J.; Zaikina, J. V.; Kovnir, K., Clathrate thermoelectrics. *Mater. Sci. Eng. R Rep.* **2016,** *108*, 1-46.

3. Owens-Baird, B.; Wang, J.; Wang, S.Y. G.; Chen, Y.-S.; Lee, S.; Donadio, D.; Kovnir, K. III-V Clathrate Semiconductors with Outstanding Hole Mobility: $Cs_8In_{27}Sb_{19}$ and $A_8Ga_{27}Sb_{19}$ (A = Cs, Rb). *J. Amer. Chem. Soc.* **2020,** *142*, 2031-2041.

4. Wang, J.; Dolyniuk, J.-A.; Kovnir, K., Unconventional Clathrates with Transition Metal–Phosphorus Frameworks. *Acc. Chem. Res.* **2018,** *51*, 31-39.

5. Tanigaki, K.; Shimizu, T.; Itoh, K.M.; Teraoka, J.; Moritomo, Y.; Yamanaka, S. Mechanism of superconductivity in the polyhedral-network compound Ba_8Si_{46}. *Nature Mater.* **2003,** *2*, 653-655.

6. Yamanaka, S.; Enishi, E.; Fukuoka, H.; Yasukawa, M. High-Pressure Synthesis of a New Silicon Clathrate Superconductor, Ba_8Si_{46}. *Inorg. Chem.* **2000,** *39*, 56-58.

7. Prokofiev, A.; Sidorenko, A.; Hradil, K.; Ikeda, M.; Svagera, R.; Waas, M.; Winkler, H.; Neumaier, K.; Paschen, S. Thermopower enhancement by encapsulating cerium in clathrate cages. *Nature Mater.* **2013,** *12*, 1096-1101.

8. Wang, J.; He, Y.; Mordvinova, N. E.; Lebedev, O. I.; Kovnir, K. The smaller the better: hosting trivalent rare-earth guests in Cu-P clathrate cages. *Chem*, **2018,** *4*, 1465-1475.

9. Kovnir, K., U. Stockert, S. Budnyk, Yu. Prots, M. Baitinger, S. Paschen, A.V. Shevelkov, Yu. Grin. Introducing a Magnetic Guest to a Tetrel-Free Clathrate: Synthesis, Structure, and Properties of $Eu_xBa_{8-x}Cu_{16}P_{30}$ ($0 \leq x \leq 1.5$). *Inorg. Chem.* **2011,** *50,* 10387-10396.

10. Plokhikh, I.V.; Khan, N.; Tsirlin, A.A.; Kuznetsov, A.N.; Charkin, D.O.; Shevelkov, A.V.; Pfitzner, A. $EuNi_2P_4$, the first magnetic unconventional clathrate prepared via a mechanochemically assisted route. *Inorg. Chem. Front.* **2020,** *7*, 1115-1126.

11. Cohn, J. L., Nolas, G. S., Fessatidis, V., Metcalf, T. H., and Slack. G. A. Glasslike Heat Conduction in High-Mobility Crystalline Semiconductors. *Phys. Rev. Lett.* **1999,** *82*, 779.

12. Paschen, S., Carrillo-Cabrera, W., Bentien, A., Tran, V. H., Baenitz, M., Grin, Yu., and Steglich, F. Structural, transport, magnetic, and thermal properties of $Eu_8Ga_{16}Ge_{30}$. *Phys. Rev. B,* **2001,** *64*, 2144041.

13. Franz, R.; Wiedemann, G. Ueber die Wärme-Leitungsfähigkeit der Metalle. *Annal. Physik* **1853,** *165*, 497-481.

14. Hill, R. W.; Proust, C.; Taillefer, L.; Fournier, P.; Greene, R. L. Breakdown of Fermi-liquid theory in a copper-oxide superconductor. *Nature,* **2001,** *414*, 711-715.

15. Tanatar, M. A.; Paglione, J.; Petrovic, C.; Taillefer, L. Anisotropic Violation of the Wiedemann-Franz Law at a Quantum Critical Point. *Science*, **2007**, *316,* 1320-1322.

16. Pfau, H.; Hartmann, S.; Stockert, U.; Sun, P.; Lausberg, S.; Brando, M.; Friedemann, S.; Krellner, C.; Geibel, C.; Wirth, S.; Kirchner, S.; Abrahams, E.; Si, Q.; Steglich, F. Thermal and electrical transport across a magnetic quantum critical point. *Nature*, **2012,** *484,* 493-497.

17. Dong, J. K.; Tokiwa, Y.; Bud'ko, S. L.; Canfield, P. C.; Gegenwart, P. Anomalous Reduction of the Lorenz Ratio at the Quantum Critical Point in YbAgGe. *Phys. Rev. Lett.* **2013,** *110,* 176402.

18. Lee, S.; Hippalgaonkar, K.; Yang, F.; Hong, J.; Ko, C.; Suh, J.; Liu, K.; Wang, K.; Urban, J. J.; Zhang, X.; Dames, C.; Hartnoll, S. A.; Delaire, O.; Wu, J. Anomalously low electronic thermal conductivity in metallic vanadium dioxide. *Science,* **2017,** *355,* 371-374.

19. Dolyniuk, J.; Wang, J.; Lee, K.; Kovnir, K. Twisted Kelvin cells and truncated octahedral cages in the crystal structures of unconventional clathrates, AM_2P_4 (A = Sr, Ba; M = Cu, Ni) *Chem. Mater.* **2015,** *27*, 4476-4484.

20. Tanatar, M. A.; Bondarenko, V. A.; Timmons, E. I.; Prozorov, R. Modular portable unit for thermal conductivity measurements in multiple cryogenic/magnetic field environments. *Rev. Sci. Instr.* **2018,** *89,* 013903.

21. Tanatar, M. A.; Ni, N.; Bud'ko, S. L.; Canfield, P. C.; Prozorov, R. Field-dependent transport critical current in single crystals of $Ba(Fe_{1-x}TM_x)_2As_2$ (TM = Co, Ni) superconductors. *Supercond. Sci. Technol.* **2010,** *23*, 054002.

22. Physical Property Measurement System, Thermal Transport Option User's Manual. Quantum Design, San Diego, 2002.

23. Wang, J.; Lebedev, O. I.; Lee, K.; Dolyniuk, J.-A.; Klavins, P.; Bux, S.; Kovnir, K., High-efficiency thermoelectric $Ba_8Cu_{14}Ge_6P_{26}$: bridging the gap between tetrel-based and tetrel-free clathrates. *Chem. Sci.* **2017,** *8*, 8030-8038.

24. Dolyniuk, J.-A.; Wang, J.; Marple, M. A. T.; Sen, S.; Cheng, Y.; Ramirez-Cuesta, A. J.; Kovnir, K., Chemical Bonding and Transport Properties in Clathrates-I with Cu–Zn–P Frameworks. *Chem. Mater.* **2018,** *30* (10), 3419-3428.

25. Dolyniuk, J.-A.; Zaikina, J. V.; Kaseman, D. C.; Sen, S.; Kovnir, K., Breaking the Tetra-Coordinated Framework Rule: New Clathrate $Ba_8M_{24}P_{28+\delta}$ (M=Cu/Zn). *Angew. Chem. Int. Ed.* **2017,** *56*, 2418-2422.

26. Ziman, J. M. Principles of the Theory of Solids, Cambridge University Press, **1964**.

27. Christensen, M.; Lock, N.; Overgaard, J.; Iversen, B. B. Crystal Structures of Thermoelectric *n*- and *p*-type $Ba_8Ga_{16}Ge_{30}$ Studied by Single Crystal, Multitemperature, Neutron Diffraction, Conventional X-ray Diffraction and Resonant Synchrotron X-ray Diffraction. *J. Amer. Chem. Soc.* **2006,** ***128***, 15657-15665.

28. He, H.; Stoyko, S.; Bobev, S. New insights into the application of the valence rules in Zintl phases - Crystal and electronic structures of $Ba_7Ga_4P_9$, $Ba_7Ga_4As_9$, $Ba_7Al_4Sb_9$, $Ba_6CaAl_4Sb_9$, and $Ba_6CaGa_4Sb_9$. *J. Solid State Chem.* **2016,** *236*, 116-122.

29. Nuss, J.; Jansen, M. $Ba_3P_3I_2$ und $Ba_5P_5I_3$: Stufenweise Oxidation von Bariumphosphid mit Iod. *Z. Anorg. Allg. Chem.* **2003,** *629*, 387-393.

30. Siggelkow, L.; Hlukhyy, V.; Fässler, T. F. $BaNi_2Ge$ and $Ca_4Ni_4Ge_3$ – Two layered Structures with $[Ni_2Ge]$ and $[Ni_4Ge_3]$ Networks. *Z. Anorg. Allg. Chem.* **2010,** *636*, 1870-1879.

31. Zhang, H.; Borrmann, H.; Oeschler, N.; Candolfi, C.; Schnelle, W.; Schmidt, M.; Burkhardt, B.; Baitinger, M.; Zhao, J.-T. Grin, Yu. Atomic Interactions in the p-Type Clathrate I $Ba_8Au_{5.3}Ge_{40.7}$. *Inorg. Chem.* **2011,** *50*, 1250-1257.

32. Novikov, V.; Pilipenko, K.; Matovnikov, A.; Mitroshenkov, N.; Plokhikh, I.; Tyablikov, A. S.; Shevelkov, A. V. Structure-Related Thermal Properties of Type-VII Clathrates $SrNi_2P_4$ and $BaNi_2P_4$ at Low Temperature. *Phys. Status Solidi B*, **2018,** *255*, 1800067.

33. Christensen, M.; Abrahamsen, A. B.; Christensen, N. B.; Juranyi, F.; Andersen, N. H.; Lefmann, K.; Andreasson, J.; Bahl, C. R. H.; Iversen, B. B. Avoided Crossing of Rattler Modes in Thermoelectric Materials. *Nature Mater.* **2008,** *7*, 811-815.

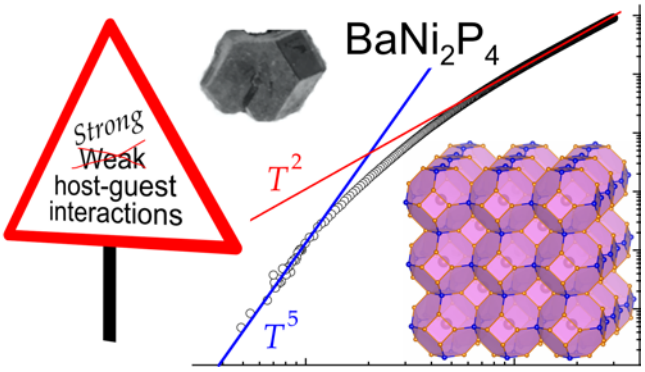
Strong
Weak
host-guest
interactions
BaNi2P4
T2
T5